June 23, 2021
Volume 143
Number 24
pubs.acs.org/JACS

JACS

JOURNAL OF THE AMERICAN CHEMICAL SOCIETY

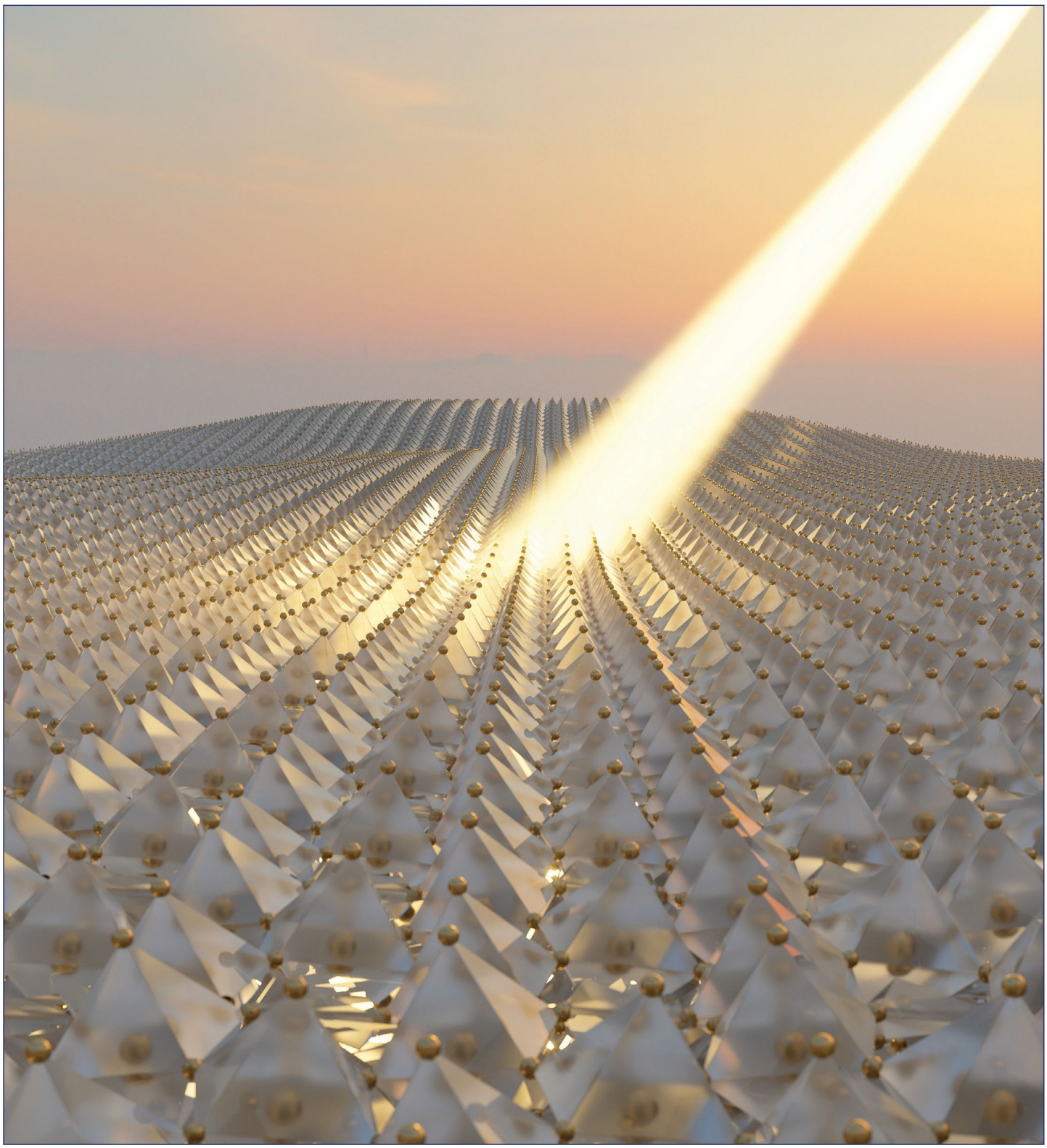

ACS Publications
Most Trusted. Most Cited. Most Read.

www.acs.org

JACS
JOURNAL OF THE AMERICAN CHEMICAL SOCIETY
pubs.acs.org/JACS
Article

Quantifying Photoinduced Polaronic Distortions in Inorganic Lead Halide Perovskite Nanocrystals

Oliviero Cannelli, Nicola Colonna, Michele Puppin, Thomas C. Rossi, Dominik Kinschel, Ludmila M. D. Leroy, Janina Löffler, James M. Budarz, Anne Marie March, Gilles Doumy, Andre Al Haddad, Ming-Feng Tu, Yoshiaki Kumagai, Donald Walko, Grigory Smolentsev, Franziska Krieg, Simon C. Boehme, Maksym V. Kovalenko, Majed Chergui,* and Giulia F. Mancini*

Cite This: J. Am. Chem. Soc. 2021, 143, 9048−9059

Read Online

ACCESS | Metrics & More | Article Recommendations | Supporting Information

ABSTRACT: The development of next-generation perovskite-based optoelectronic devices relies critically on the understanding of the interaction between charge carriers and the polar lattice in out-of-equilibrium conditions. While it has become increasingly evident for $CsPbBr_3$ perovskites that the Pb−Br framework flexibility plays a key role in their light-activated functionality, the corresponding local structural rearrangement has not yet been unambiguously identified. In this work, we demonstrate that the photoinduced lattice changes in the system are due to a specific polaronic distortion, associated with the activation of a longitudinal optical phonon mode at 18 meV by electron−phonon coupling, and we quantify the associated structural changes with atomic-level precision. Key to this achievement is the combination of time-resolved and temperature-dependent studies at Br K and Pb L_3 X-ray absorption edges with refined *ab initio* simulations, which fully account for the screened core-hole final state effects on the X-ray absorption spectra. From the temporal kinetics, we show that carrier recombination reversibly unlocks the structural deformation at both Br and Pb sites. The comparison with the temperature-dependent XAS results rules out thermal effects as the primary source of distortion of the Pb−Br bonding motif during photoexcitation. Our work provides a comprehensive description of the $CsPbBr_3$ perovskites' photophysics, offering novel insights on the light-induced response of the system and its exceptional optoelectronic properties.

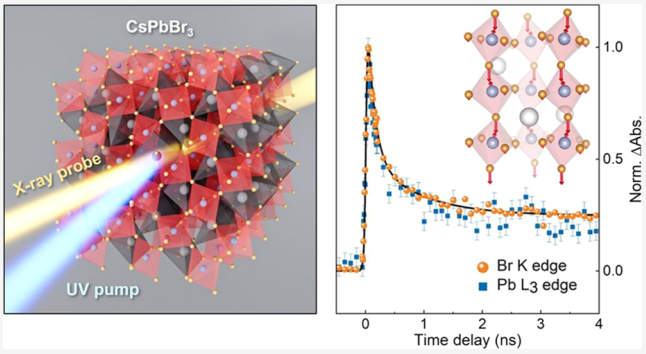

INTRODUCTION

Lead halide perovskites are rapidly emerging as excellent candidates for optoelectronic applications, such as photovoltaics, light-emitting diodes,[1] lasers,[2] photodetectors,[3] polariton devices,[4] and quantum light sources,[5] thanks to their outstanding performances and low fabrication costs.[6] These materials are characterized by facile processing routes, leading to defect-tolerant systems with widely tunable band gaps, high photoluminescence (PL) quantum yields, and narrow emission lines. Their potential stems from their extraordinarily long carrier lifetimes and diffusion lengths,[7,8] which are in apparent contrast with previously reported low charge mobility[9] and lattice dynamical disorder.[10]

The $APbX_3$ perovskite structure comprises a Pb−X (X = Cl, Br, I) inorganic framework made of flexible corner-sharing octahedra, with Pb^{2+} cations surrounded by six halide anions, characterized by low-frequency phonons and a pronounced anharmonicity.[11−15] The A^+ cations, either inorganic (Cs^+) or organic (methylammonium, MA^+, or formamidinium, FA^+), fill the voids between PbX_6 octahedra. Distinct orthorhombic, tetragonal, and cubic phases were identified in these systems, with phase transition temperatures varying with the cation composition.[13,16−18] In $CsPbBr_3$ nanocrystals (NCs), the phase diagram is characterized by a room-temperature orthorhombic *Pnma* crystalline group, with a transition to a tetragonal $P4\bar{m}bm$ group between 50 and 59 °C, and a higher temperature transition to a cubic $Pm\bar{3}m$ group between 108 and 117 °C.[13]

Recent temperature-dependent studies revealed competitive mechanisms underlying the thermal response in lead halide perovskites. Pair distribution function (PDF) analysis from X-ray powder diffraction in organic perovskites at room temperature showed significant internal local distortions of the PbX_6 octahedra.[19] The degree of these distortions was found to increase with the temperature in $MAPbBr_3$.[20] In $CsPbX_3$ NCs,

Received: March 3, 2021
Published: June 2, 2021

Downloaded via UNIV DEGLI STUDI DI PAVIA on May 16, 2023 at 13:37:43 (UTC).
See https://pubs.acs.org/sharingguidelines for options on how to legitimately share published articles.

ACS Publications
© 2021 The Authors. Published by American Chemical Society

https://doi.org/10.1021/jacs.1c02403
J. Am. Chem. Soc. 2021, 143, 9048−9059

structural defectiveness was revealed and ascribed to twin boundaries, whose density increases with temperature and leads to an apparent higher-symmetry structure that does, however, not correspond to the $Pm\bar{3}m$ cubic phase.[12] High energy resolution inelastic X-ray scattering and PDF studies on $MAPbI_3$ pointed to the presence of thermally active anharmonic soft modes at 350 K,[11] and local polar fluctuations among different noncubic structures were confirmed in a low-frequency Raman study on $MAPbBr_3$ and $CsPbBr_3$ perovskites.[15]

The peculiar lattice flexibility of lead halide perovskites also critically underpins their photodynamics. Time-resolved optical studies were conducted to understand key aspects of the early dynamics of the system.[21−23] Several works suggested the presence of polarons, i.e., charge carriers dressed by lattice distortions, in order to explain the time-resolved optical signals[14,24−27] and transport properties.[28] Polaron formation was shown to generally occur through the Fröhlich mechanism,[29] which corresponds to a Coulomb interaction between the charge carriers and the macroscopic electric field created by the activation of longitudinal optical (LO) phonons.[30,31]

Although the polaron hypothesis was frequently invoked to rationalize experimental observations in both organic and inorganic perovskites, the quantification of the associated local structural rearrangement is still missing. In hybrid organic−inorganic lead halide perovskites, local distortions around the Pb[32] and Br[33] sites were separately reported in time-resolved X-ray absorption spectroscopy (TR-XAS) studies and ascribed to polaron formation, but an unambiguous identification of the associated structural fingerprint was not provided. Ultrafast electron diffraction on a $MAPbI_3$ thin film showed evidence of local rotational disorder of the PbI_6 octahedra arising from optical excitation, as a consequence of hot carrier−phonon coupling.[34] Only recently was the presence of a dynamically expanding polaronic strain structurally identified in an $MAPbBr_3$ single crystal with time-resolved diffusive X-ray scattering.[35]

In all-inorganic lead halide perovskites the picture is still unclear. In a previous TR-XAS study of photoexcited $CsPbBr_3$ and $CsPb(BrCl)_3$ NCs at the Br K-, Pb L_3-, and Cs L_2-edges[36] carried out at a synchrotron, it was suggested that hole polarons form within the time resolution of the experiment ($\leq$100 ps), around Br centers, with the halide ion turning into a neutral halogen, while electrons would be delocalized in the conduction band (CB). Additionally, the Cs sites did not show any response to photoexcitation. In a more recent time-resolved X-ray diffraction study (TR-XRD) at similar fluences, namely, between 2.5 and 12 mJ/cm^2, the lattice response upon photoexcitation was interpreted in terms of transient amorphization from a crystalline structure.[37] In both studies, however, the local structural distortion was invoked to rationalize experimental data in a qualitative way, rather than a quantitative one. A recent angle-resolved photoelectron spectroscopy (ARPES) study concluded to the existence of hole polarons based on the increase of the hole effective mass in $CsPbBr_3$ single crystals caused by electron−phonon coupling and it identified a specific LO phonon at 18 meV as the most coupled mode with the charge carriers.[38]

In this work we demonstrate that, in $CsPbBr_3$ NCs, the 18 meV LO phonon mode is underpinning the structural distortion induced upon photoexcitation, and we quantify the polaronic nuclear displacements with atomic precision. Specifically, we conducted a TR-XAS study at the Br K *and* Pb L_3 absorption edges and we found that photoexcitation indeed induces polaron formation around Br centers, which also determines the response of Pb centers. We performed band structure calculations in which—to our knowledge for the first time in TR-XAS studies—the possible structural distortions are *a-priori* selected on a physical basis, fully accounting for core-hole final state effects on the XAS spectra. By comparing these accurate simulations to our experimental results, we identify the local PbX_6 octahedra bond distortions that contribute to the polaronic photoresponse. Additionally, we clarify the fundamental difference underlying optical and thermal activation in $CsPbBr_3$ NCs: our temperature-dependent XAS experiments result in quantitatively different spectral modifications compared to the optical activation, thereby excluding heat as the primary source of distortion of the Pb−Br bonding motif upon photoexcitation.

METHODS

Br K-edge and Pb L_3-edge spectra have been recorded in the pre-edge and the XANES (X-ray absorption near edge structure) regions upon light or thermal activation of $CsPbBr_3$ NCs. The pre-edge region contains bound−bound core-to-valence transitions and is therefore sensitive to the density of unoccupied valence orbitals. The XANES includes the region just above the ionization limit (i.e., the edge). It is characterized by single and multiple scattering events of the photoelectron, and, hence, it contains information about the bond distances and angles to the nearest-neighbor atoms around the probed site.[39,40] In its time-resolved implementation, the photoinduced changes of the TR-XAS spectrum reflect transient structural and electronic modifications at the probed sites and in their local environment.[41]

The TR-XAS experiments were conducted at the 7ID-D beamline at the Advanced Photon Source (APS) of the Argonne National Laboratory.[42,43] A schematic representation of this experiment is shown in Figure 1. The sample consisted of long-chain zwitterion-

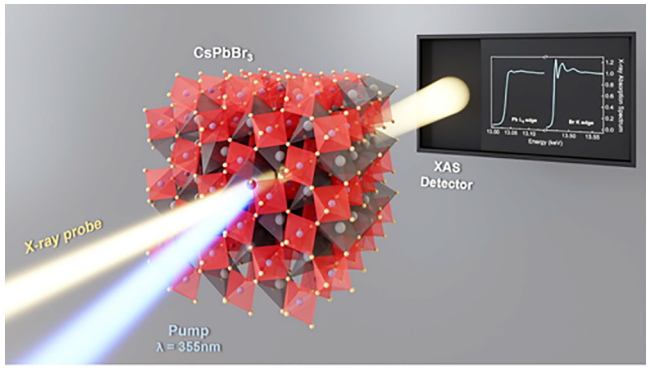

Figure 1. Ultrafast element-selective probing of optically induced polaronic distortions in $CsPbBr_3$ perovskite NCs. Schematic layout of the experiment. TR-XAS was conducted on long-chain zwitterion-capped $CsPbBr_3$ NCs dispersed in a toluene solution with a concentration of 5.8 mg/mL and flowed through a flat jet. The laser pump (355 nm) and the X-ray probe at the Br K-edge (13.450−13.570 keV) and Pb L_3-edge (13.000−13.140 keV) were in an almost collinear geometry. Courtesy of Balázs Őrley. Please note: Image also appears in the TOC/Graphical Abstract.

capped $CsPbBr_3$ perovskite NCs with cuboidal shape (side length 10 ± 2 nm) and high PL quantum yields.[44] Above band gap photoexcitation was performed using a Duetto laser at a photon energy of 3.49 eV (i.e., 1.1 eV above the direct band gap excitation), a repetition rate of 1.304 MHz, 10 ps pulse duration, and with a fluence of 8.8 mJ/cm^2, in the linear response regime. The photoinduced changes in the sample were probed at the Br K-edge (13.45−13.57 keV) and Pb L_3-edge (13.00−13.14 keV), with ∼80 ps time resolution.

https://doi.org/10.1021/jacs.1c02403
J. Am. Chem. Soc. 2021, 143, 9048−9059

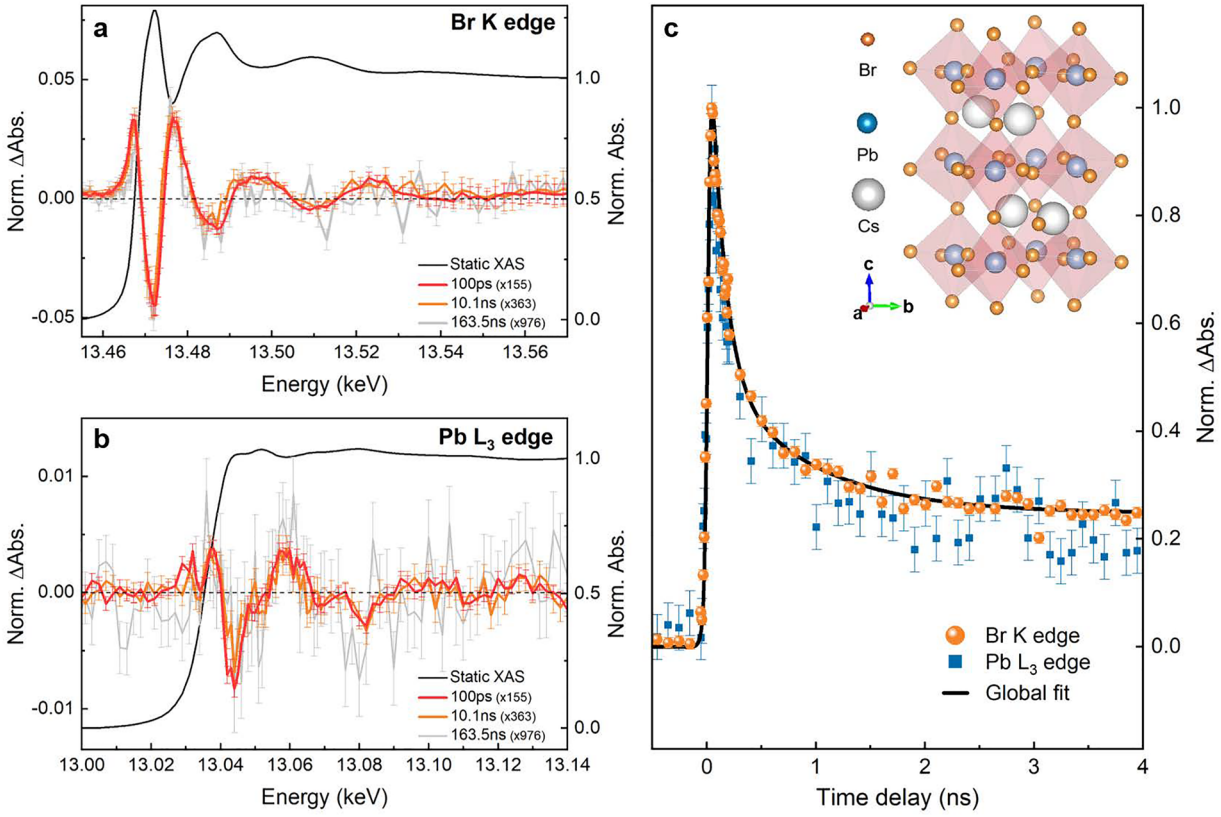

Figure 2. X-ray absorption energy and time traces. (a) Br K-edge and (b) Pb L_3-edge XAS spectra: steady-state (black) and energy transients at 100 ps (red, ×155), 10.1 ns (yellow, ×363), and 163.5 ns (gray, ×976) time delays. The error bars correspond to the standard error of the measurements. (c) TR-XAS time traces at the Br K-edge (13.472 keV, orange), Pb L_3-edge (13.043 keV, light blue), and the exponential fit (black). The error bars were computed as the error propagation of the pumped and unpumped scans, calculated as the square root of the total single-photon counts. Inset: Graphical representation of *Pnma* orthorhombic $CsPbBr_3$.[68] The Br, Pb, and Cs atoms are respectively reported as orange, light blue, and gray spheres.

Comparative temperature-dependent Br K-edge and Pb L_3-edge static XAS was conducted at the SuperXAS beamline of the Swiss Light Source (SLS). The experiments were performed on dry $CsPbBr_3$ NCs enclosed in a thermostated cell holder. The thermal response of the system was monitored in the temperature range between 25 and 140 °C, where effects ascribed to either an increase in the NCs local structural disorder[12] or the occurrence of orthorhombic-tetragonal-cubic phase transitions[13,16] had previously been reported. Moreover, we acquired for each temperature step XRD patterns at 12.9 keV, below both absorption edges, to track longer-range structural changes and to assess the overall quality of the sample.

We performed first-principles calculations using the Quantum ESPRESSO distribution,[45,46] based on density functional theory (DFT) and plane-wave and pseudopotentials techniques. The Perdew−Burke−Ernzerhof functional[47] was used to describe electronic exchange−correlation effects. The electron−ion interaction was modeled using ultrasoft pseudopotentials from the PS-library.[48] The projected density of states (p-DOS) was computed across the band gap. XANES Br K-edge spectra were simulated with the XSpectra code[49,50] of Quantum ESPRESSO, explicitly accounting for the screened core-hole effect in separate supercell calculations for each nonequivalent Br atom and calculating the average Br K-edge spectra. XANES Pb L_3-edge calculations were not carried out due to the limitations in the explicit inclusion of a screened core-hole in describing holes with nonzero orbital momentum,[51] as in the case of the Pb $2p_{3/2}$ orbital. Details about all experimental methods, the data acquisition scheme, and the computational methods and DOS calculations are described in the Supporting Information (SI).

RESULTS

TR-XAS. The steady-state Br K-edge and Pb L_3-edge spectra, normalized to the last data point of the postedge region, are shown in Figure 2a and b (black solid line). Our calculations of the p-DOS show that the top of the valence band (VB) is composed of Br 4p orbitals, with a non-negligible proportion of Pb 6s orbitals and a minor contribution of Pb 6p orbitals, while the CB is largely dominated by the Pb 6p orbitals (see the SI).

The photoinduced changes are reflected in the transient spectra, defined as the difference of the excited minus unexcited XAS spectra, and shown for UV pump/X-ray probe time delays of 100 ps (red), 10.1 ns (yellow), and 163.5 ns (gray). The Br transient spectra (Figure 2a) were scaled by the inverse of the absolute area underlying the curves, i.e., ×155 (100 ps), ×363 (10.1 ns), and ×976 (163.5 ns). The same scaling factors were used for the Pb transients (Figure 2b, details in the SI). Notably, even though the amplitude of the TR-XAS decays over time, the profiles of both Br and Pb transient spectra remain unchanged.

The Br K-edge transients show prominent peaks at the pre-edge (13.4675 keV), main-edge (13.472 keV), and postedge (13.4765 keV) regions. The first feature was ascribed to the opening of a new 1s−4p channel following the creation of holes in the VB upon photoexcitation.[36] Such a scenario also implies a blue shift of the edge, and, indeed, the second and third features could partially be reproduced in the difference spectrum of the blue-shifted ground-state spectrum minus the unshifted one. However, this qualitative approach does not account for all the modulations that show up in the above-edge region, which

https://doi.org/10.1021/jacs.1c02403
J. Am. Chem. Soc. 2021, 143, 9048−9059

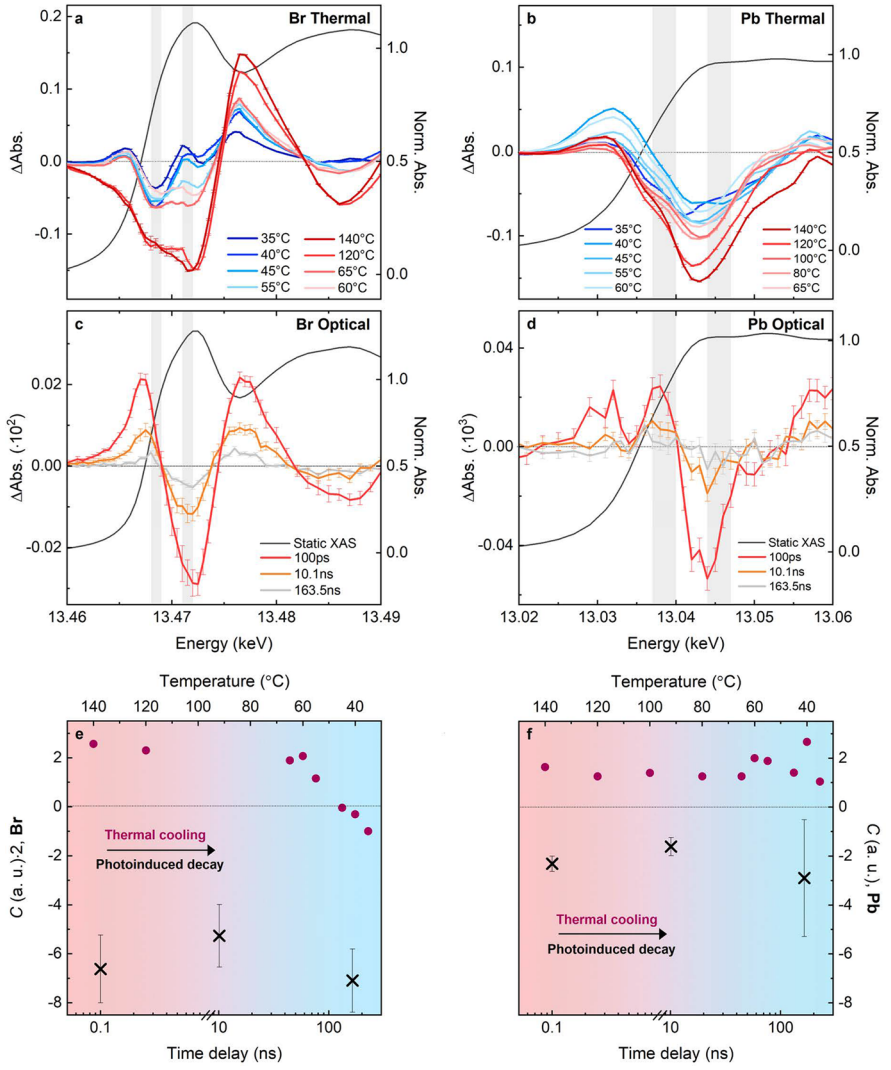

Figure 3. Comparison between photoinduced and thermally activated XAS transition in $CsPbBr_3$ at the Br K-edge and Pb L_3-edge. (a) Br K-edge steady-state (dark gray) and temperature-dependent XAS differences from 35 to 140 °C (respectively from blue to red) and (b) Pb L_3-edge steady-state (dark gray) and temperature-dependent XAS differences from 35 to 140 °C (respectively from blue to red). In both panels, the XAS differences were computed by subtracting the 25 °C spectrum from the temperature-dependent XAS spectra. Before performing the differences, all steady-state temperature-dependent spectra were baseline corrected and scaled by their underlying areas (consistently with the data treatment of time-resolved spectra). A three-point adjacent averaging of the spectra was performed to better track the evolution of the spectral shape as a function of the temperature. (c) Br K-edge steady-state (dark gray) and pump−probe spectra at 100 ps (red), 10.1 ns (yellow), and 163.5 ns (gray) and (d) Pb L_3-edge steady-state (dark gray) and pump−probe spectra at 100 ps (red), 10.1 ns (yellow), and 163.5 ns (gray). The steady-state spectra in panels (a), (c) and (b), (d) show the same spectral shapes, accounting for their different energy resolution. (e) Br K-edge comparison parameter *C* as a function of the temperature (purple dots, top axis) and pump−probe time delay (black crosses, bottom axis), defined as the ratio of the averaged XAS difference in the energy interval 13.471−13.472 keV and 13.468−13.469 keV, corresponding to the shaded areas in panels (a) and (c). (f) Pb L_3-edge comparison parameter *C* as a function of the temperature (purple dots, top axis) and pump−probe time delay (black crosses, bottom axis), defined as the ratio of the averaged XAS difference in the energy interval 13.044−13.047 keV and 13.037−13.040 keV, corresponding to the shaded areas in panels (b) and (d). Br *C* values for both thermal and optical data sets were multiplied by a factor of 2 in order to enable a straightforward comparison between Br and Pb results in panels (e) and (f).

generally point to photoinduced structural changes (further details in the SI). We will address these later, using *ab initio* calculations and demonstrating their connection with photoinduced lattice distortions. The Pb L_3-edge steady-state spectrum exhibits featureless edge and XANES regions. The transients are characterized by two positive features in the preedge region (13.031 and 13.038 keV), a negative peak at the edge position (13.043 keV), and a positive peak in the postedge region (13.060 keV). The reduction of Pb centers upon photoexcitation of the electrons in the CB, which is mainly composed by Pb p orbitals, is not compatible with the transient line shape, as discussed by Santomauro et al.[36] The appearance of pre-edge features in the transient traces can only be explained by the opening of new channels from the 2p core orbitals. Indeed, due to hybridization, depleting the VB affects not only the Br centers but also the Pb ones, according to the computed p-DOS (see SI). Core-to-valence transitions can occur into the Pb 6s orbitals, which have a non-negligible contribution toward the top of the VB. Above the edge, the transient features are due to photoinduced structural changes. Because the Pb atoms are affected by the structural distortion around the Br centers (see

https://doi.org/10.1021/jacs.1c02403
J. Am. Chem. Soc. 2021, 143, 9048−9059

below), it is likely that the above-edge features of the Pb L_3 absorption transient in part reflect the latter.

The decay kinetics at both Br and Pb main edges are shown in Figure 2c. The traces were normalized to their maximum value, allowing a straightforward comparison of the time-resolved signal of both centers. It is clear that both traces show the same temporal evolution within the noise level. The data were analyzed following a global fit procedure for both traces. The best fit results were obtained with a biexponential decay function and a flat offset, which persists up to 130 ns, the time limit explored in our time traces (see the SI). The fit function was convoluted with a Gaussian profile (σ = 45 ps), representing the instrument response function of our measurements. The recorded time constants (pre-exponential factors) are τ_1 = 120 ± 20 ps (60%), τ_2 = 900 ± 300 ps (21%), and an offset (infinite times of 19% amplitude). Specifically, the fast time component τ_1 is compatible with Auger recombination, where an electron in the CB and a hole in the VB recombine, in a nonradiative process, transferring their energy to a third carrier. Supporting this interpretation, recent fluence-dependent PL and transient absorption studies on $CsPbBr_3$ NCs reported Auger recombination acting on this time scale.[52,53] τ_2 is ascribed to the radiative recombination of the photoexcited charge carriers, i.e., holes from the VB and electrons from the CB, in general agreement with PL studies.[44,54]

Thermal XAS. Given the ongoing debate about photoinduced electronic and thermal effects[37] and considering that our pump pulse deposits an excess energy of the photocarriers of ∼1 eV, it is important to disentangle electronic from thermal effects in the photoinduced response presented here.

In our pump−probe experiment, the hot carriers generated by the pumping process dissipate their excess energy through carrier thermalization in the sub-100 fs regime[21] and, immediately after, by charge carrier cooling on sub-picosecond time scales.[55] These events determine impulsive heating of the crystalline lattice. If the energy deposited in the system is sufficiently high, this process might translate into impulsively activated orthorhombic-tetragonal-cubic phase transitions.[13] At later time scales, the hot lattice relaxes through heat transfer to the solvent and/or the ligands. In ligand-stabilized colloidal NCs in solution this process should be completed in sub-nanosecond time scales,[56] due to the efficient vibrational coupling between the NC, the ligands, and the solvent molecules. Our TR-XAS experiment looks at the system relaxation in time scales from 80 ps onward after photoexcitation, i.e., when the thermal equilibration of the lattice with the surrounding bath has already initiated. At these time scales, the photoinduced relaxation of the system and its purely thermal and temperature-dependent responses can be directly compared. This assumption can be harnessed to verify whether the optically induced relaxation coincides with thermodynamic lattice cooling.

Figure 3a,b show the thermal difference spectra at the Br K- and the Pb L_3-edges (full thermal spectra are available in the SI). These are obtained by subtracting the 25 °C spectrum from the *T*-dependent XANES spectra. Figures 3c,d show the unscaled pump−probe difference spectra at 100 ps (red), 10.1 ns (yellow), and 163.5 ns (gray) for each absorption edge. The thermal difference spectra at the Br K-edge (Figure 3a) display an intensity change through the thermal gradient, with an overall area decrease in the energy range 13.466−13.478 keV on lowering the temperature from 140 °C to 25 °C. Particularly, the features at 13.468 and 13.472 keV have two different temperature dependences, the former becoming dominant for temperatures below 65 °C. Main differences between photoinduced and thermal data sets can be found in the Br K pre-edge region. Specifically, the negative feature at 13.468 keV found in the thermal data set is absent in the pump−probe spectra, which instead are characterized by a positive peak centered around 13.4675 keV. In the case of Pb, thermal difference spectra in Figure 3b display a broad negative feature covering the 13.035−13.053 keV spectral range, whose intensity uniformly decreases on lowering the temperature, and a single pre-edge feature centered at 13.032 keV, with intensity increasing upon temperature decrease. In contrast and as already discussed, the pump−probe Pb spectra show two pre-edge peaks, respectively at 13.031 and 13.038 keV, whose intensity decreases as a function of time delay.

To quantify overall spectral changes as a function of either temperature or optical excitation, at both edges, we introduce a comparison parameter *C* defined as

$$C = \sum_{E_i} I(E_i) / \sum_{E_j} I(E_j)$$

with $I(E_i)$ and $I(E_j)$ being the spectral intensities at the energy points E_i and E_j in the main-edge and pre-edge regions, respectively. In Figure 3a−d (gray areas), E_i(Br) = 13.471−13.472 keV; E_j(Br) = 13.468−13.469 keV; E_i(Pb) = 13.044−13.047 keV; and E_j(Pb) = 13.037−13.040 keV. The indicated intervals comprise equally spaced energy points. Figure 3e,f show the parameter *C* for Br and Pb, respectively: it expresses the relative intensity ratio between two spectral regions of the same data set, and it describes the entity of XAS spectral shape changes through a temperature gradient (purple dots) or upon photoexcitation (black crosses).

Within the error bars, *C* values are constant in the pump−probe case for either Br or Pb, in agreement with the spectral evolution of the TR-XAS signal. Indeed, we observe a synchronous systems's response throughout the TR-XAS spectrum in its decay to the ground state. We remark that negative values of *C* are due to the presence of the pre-edge and main-edge features that have opposite signs, respectively, at the energies 13.4675 and 13.472 keV for the Br K-edge and at 13.038 and 13.044 keV for the Pb L_3-edge. Starting from 140 °C, the *C* parameter for the Br thermal differences has stable positive values for temperatures down to 60 °C and undergoes a progressive change from positive to negative values on lowering the temperature in the interval 60−35 °C, due to line shape modifications in the edge region. Instead, Pb thermal differences show positive *C* values at all temperatures, which originate from the negative sign of pre-edge and main-edge features. Since both features decrease in amplitude upon temperature decrease, Pb *C* values remain essentially unchanged with the thermal gradient.

On the basis of the radically different behavior of the *C* parameter for the optical and thermal data sets, we can safely conclude that the photoresponses at the Pb and Br edges reported here are not affected by thermal effects, which likely occur on shorter time scales than our temporal window, as discussed in the following. Thus, we rule out the hypothesis that the photoexcited state corresponds to thermally driven lattice changes.[37]

Theoretical Simulations: Photoinduced Polaronic Distortion. The XAS spectrum reflects the probability of an electronic excitation from a core orbital to the unoccupied states of the system that lie at higher energies than the Fermi level.

https://doi.org/10.1021/jacs.1c02403
J. Am. Chem. Soc. 2021, 143, 9048−9059

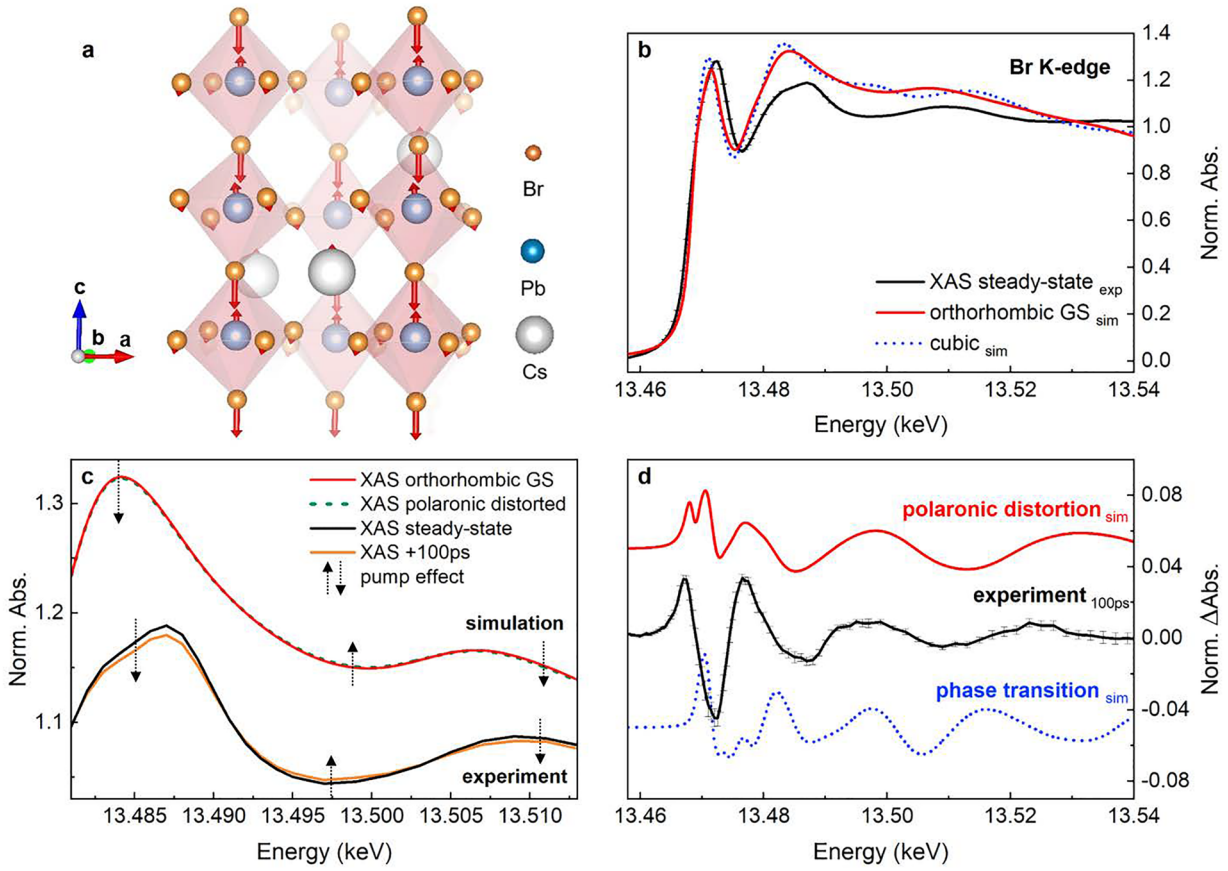

Figure 4. Theoretical *ab initio* calculations of Br K-edge XAS spectra for the ground and structurally distorted states in $CsPbBr_3$. (a) Schematics of the atomic displacements related with the 18 meV LO phonon mode. (b) Steady-state experiment (black, normalized for the last energy point), ground-state orthorhombic simulation (red solid line, scaling factor ×2550), and cubic simulation (blue dashed line, scaling factor ×2550). (c) Ground-state orthorhombic simulation (red, scaling factor ×2550), orthorhombic distorted along the 18 meV LO phonon mode (green dashed line, scaling factor ×2550), and unpumped (black, normalized for the last energy point) and pumped (yellow, 100 ps time delay, normalized for the last energy point) experimental spectra. (d) Experimental transient at 100 ps (black) and simulated pump−probe obtained as distorted orthorhombic minus pristine orthorhombic spectra (polaronic distortion, red) and cubic minus orthorhombic spectra (phase transition, blue dashed line). All spectra were scaled by the absolute area underlying the curves and the simulated pump−probe additionally multiplied by a factor 70 to enable the comparison with the experiment.

Hence, the first-principles description of XANES spectra requires the computation of highly localized initial orbitals and of the unoccupied conduction states, the latter in the presence of a screened core-hole, since it reflects the possible final states with a missing core electron.

In condensed matter systems, this level of accuracy is retrieved relying on band structure calculations, where the effect of the screened core-hole is explicitly accounted for as, for example, in supercell simulations.[57,58] Band structure calculations also allow access to the phonon spectrum of the system, the atomic displacements occurring upon phonon mode activation, and the electron−phonon coupling between the charge carriers and the lattice degrees of freedom. To date XAS spectra of several solid-state systems have been computed using *ab initio* methods, which rely on real-space atomic clusters, especially for the simulation of excited-state spectra.[32,59−61] In these cases, the interest was focused on determining the local structural distortions in the photoexcited system, as in the case of charge carriers trapping, rather than understanding the origin of its structural response in the presence of charge carriers, which requires electron−phonon coupling calculations.

First-principles computations of pump−probe spectra are generally performed either using *a-posteriori* strategies, i.e., gradually modifying the local structure of a small atomic cluster until the best agreement between the simulation and the experiment is achieved,[32,59,61] or selecting *a-priori* specific subsets of configurations, where stricter constraints are imposed on a physical basis.[60] Here, to our knowledge for the first time in TR-XAS, we adopt an approach based on *ab initio* calculations performed under periodic boundary conditions with an *a-priori* selection of the structurally distorted states. Consistent with the phase diagram of $CsPbBr_3$ perovskite,[13,16] we computed the ground-state considering the atomic positions of the *Pnma* orthorhombic cell, as derived from room-temperature XRD.[16] The lattice perturbation caused by the optical pump was then simulated following two possible scenarios.

First we consider the scenario, ruled out experimentally, in which a thermally induced phase transition to an ordered $Pm\bar{3}m$ cubic state might occur. In fact, we estimated an upper limit of $\Delta T \approx 120$ °C to the impulsive heating generated by our pump pulse (see the SI), which, in the absence of lattice cooling and consistent with the $CsPbBr_3$ phase diagram, would lead the system from the orthorhombic to the cubic phase. For our simulation we use the atomic coordinates available in the literature.[16] Second, we consider a polaronic distortion induced by electron−hole pair excitation, introducing a structural

https://doi.org/10.1021/jacs.1c02403
J. Am. Chem. Soc. 2021, 143, 9048−9059

modification along the 18 meV phonon mode, which is the most strongly coupled to the charge carriers via electron−phonon coupling.[38] The structural modification caused by the aforementioned process is schematized in Figure 4a. Key to this method is the adoption of a band structure calculation, which allows (i) identifying the phonon mode with the strongest electron−phonon coupling and (ii) introducing the phonon distortion in the periodic lattice, thereby approximating the large polaron spatial extension over multiple unit cells, in agreement with the literature.[14,38] Electronic nonequilibrium effects following the optical excitation were not included in the calculations, being too computationally intensive in the presence of an explicit core-hole description.

Figure 4b compares the simulated Br K-edge absorption spectra for the orthorhombic ground state (red solid) and the cubic state (blue dots) with the experimental steady-state spectrum (black solid). The three X-ray absorption spectra are characterized by a first peak arising from the Br 1s−4p electronic transition around 13.472 keV. The above-edge spectral modulations for the calculated orthorhombic ground state best reproduce the experiment, as expected from the $CsPbBr_3$ perovskite phase diagram, which is characterized by a *Pnma* orthorhombic symmetry at room temperature. The simulated spectrum for the cubic phase shows a modulation mismatch with respect to the experiment, which is prominent in the 13.492−13.505 keV energy range.

Figure 4c zooms into the above-edge region beyond 13.480 keV of the experimental pumped and unpumped spectra (respectively yellow and black traces) and for the simulated orthorhombic ground state and the polaronic distorted state (respectively red and dashed-green traces). Even though the photoinduced changes are more pronounced in the experiment, the simulation faithfully follows the photoinduced spectral modification, with intensity depletions of the 13.485 and 13.508 keV maxima and an intensity increase of the 13.497 keV minimum.

Figure 4d shows the simulated pump−probe signals obtained subtracting the XAS spectrum of the orthorhombic ground state from the XAS spectrum due to the polaronic distortion (red solid) as well as from the cubic phase XAS spectrum (blue dots). The comparison of the difference curves allows removing possible systematic errors of our *ab initio* calculation for both ground and excited states. Above the edge, the experimental pump−probe spectrum at 100 ps shows very good agreement in both position and relative amplitude assuming a polaronic lattice distortion generated by the optical activation of the 18 meV LO phonon within the polar inorganic lattice. On the other hand, there is a clear disagreement with the simulation that assumes the phase transition to the $Pm\bar{3}m$ cubic structure. We highlight that the XAS simulation for the orthorhombic−cubic phase transition does not reproduce the spectral line shape of the 120 °C minus 25 °C thermal difference reported in Figure 3a either. This result is analyzed in a separate work.

We remark that the residual deviations between the simulated polaronic distortion and the experimental pump−probe spectra (Figure 4d) can be rationalized considering that electronic effects caused by the optical pump are absent in the calculation. Indeed, the edge region is particularly sensitive to photoinduced changes of the unoccupied DOS of the system. Relying on the one-electron approximation, in Br K-edge transitions the initial and final states differ by the presence of a core-hole in a 1s Br orbital and a photoelectron above the Fermi level. Due to the localization of the 1s orbitals on Br atoms, the Br K-edge transition probability is non-negligible only for final states where the photoelectron has a significant character of the Br absorbing atom, which are present in both the VB and CB (see the SI). When the band occupancy is perturbed by the optical pump, the Br XANES in the edge region is also modified.

DISCUSSION

The comparison of optical XAS study with temperature-dependent XAS measurements rules out a dominant photo-induced thermal effect in the TR-XAS response. Indeed, if the evolution of the pump−probe spectral line shape reflected the lattice cooling following impulsive heating, a change in the TR-XAS signal intensity and line shape similar to Figure 3a,b should be expected. However, this is not observed in the transients reported in Figure 3c,d. Furthermore, this discrepancy is confirmed by the differences in the *C* parameters of Figure 3e,f between the thermal and optical data sets. Thus, even though a significant heat deposition could occur under our experimental conditions (see the SI for calculations), a thermal origin of the transient signal can hardly justify the strong difference between the time evolution of the pump−probe signal and the changes expected for thermal cooling.

In ligand-stabilized colloidal NCs, heat transport is known to be determined by the organic/inorganic interface rather than the thermal conductivity of the inorganic core of the NC.[62] In CdSe NC systems, the heat loss from the ligand−NC complex to the bath was observed in 150−320 ps, depending on the solvent.[56] Considering the similarity of the ligand-capped CdSe system and our NCs in size, ligand composition, low-energy NC phonon spectrum, fast thermalization dynamics,[56,63] and the main role of the ligand−solvent coupling to the cooling process, analogous time scales are expected for our $CsPbBr_3$ NCs in solution. Relying on Newton's law to describe the NC lattice cooling and assuming a relatively slow $\tau_{cooling}$ of 300 ps, an initial $\Delta T \approx 120$ °C temperature would quickly drop to smaller values, e.g., $T_{NC}(t = 600\ \text{ps}) \approx 40$ °C.

This prediction is in stark contrast with the persistency of the TR-XAS signal over time, which preserves the same line shape at the Br and Pb edges up to the longest time delay measured in our pump−probe experiment, namely, 163.5 ns. We conclude that heat dissipation in zwitterion-capped $CsPbBr_3$ perovskite NCs should be complete in shorter time scales than our TR-XAS time resolution, not affecting the pump−probe measurements. Notably, similar results were reported in a Pb L_3-edge TR-XAS investigation on $MAPbBr_3$ ligand-capped NCs in solution,[32] where the significant heat load caused by the pump energy deposition into the NC lattice was argued to be dissipated in time scales shorter than 100 ps.

The light-activated structural modification is not compatible with a cubic crystalline structure, nor is it due to disorder, amorphization, or melting caused by thermal effects. Our theoretical analysis clarifies key aspects of the photoinduced response of $CsPbBr_3$ perovskite NCs, ascribing the excited-state structural changes to the presence of distinct polaronic distortions that the XAS simulation specifically identifies. Indeed, the atomic displacements of the Pb−Br framework are traced back to the distortion of the 18 meV LO phonon mode, which is the most strongly responsive to the charge carriers via electron−phonon coupling. Strong electron−phonon coupling in lead halide perovskites was demonstrated in the electronic structure of $CsPbBr_3$ single crystals, where signatures of large hole polarons were identified by ARPES and attributed to the activation of the same LO phonon mode.[38] Moreover, previous

https://doi.org/10.1021/jacs.1c02403
J. Am. Chem. Soc. 2021, 143, 9048−9059

time-domain results based on the optical Kerr effect,[14] electronic resonant and nonresonant impulsive vibrational spectroscopy,[25] ultrafast THz studies,[27] and 2D electronic spectroscopy[24] were rationalized in terms of polaron formation in organic and inorganic perovskites. Polaronic strain was also invoked as the primary driving force of light-induced phase separation in multihalide perovskites, explaining the reversibility of the process, its dependence on the number of photocarriers, and the self-limiting size of the domains.[64] The importance of electron−phonon coupling on the $CsPbBr_3$ electronic response was also confirmed by PL investigations[65] and time-resolved 2D electronic spectroscopy,[26] pointing to a relevant influence of LO phonon modes with energies between 16 and 19 meV, and attributed to the lead halide inorganic framework, consistently with our findings.

Thanks to the agreement with the TR-XAS experimental results, our simulations provide a compelling atomic-level description of the polaronic distortion. As depicted in Figure 4a, the distortion along the 18 meV phonon mode implies that the Pb−Br bonds are asymmetrically shortened along the orthorhombic *c*-axis, moving Pb cations out of the octahedral inversion center and substantially displacing the axial Br nuclei from their equilibrium position, whereas the equatorial Br centers and the Cs ions are marginally affected. Specifically, the photoinduced displacement of the axial Br atoms along the *c*-axis ($Pb-Br_{axial}$ equilibrium bond distance = 2.958 Å) is 6 times larger than the equatorial Br atoms ($Pb-Br_{equatorial}$ equilibrium bond distance = 2.964 Å) and 2.5 times more pronounced than the Pb off-center displacement. The postedge modulations observed in the Pb L_3-edge transients can thus be explained by the displacements of the Pb and Br centers caused by the photogenerated polaronic distortion. Notably, the previously reported absence of a photoinduced structural response from the Cs centers[36] also agrees with this finding. Indeed, in all-inorganic perovskites the A^+ cation allocated in the lattice cuboctahedral voids is largely mobile and its dynamics is essentially decoupled from the inorganic Pb−X framework.[10] Further supporting the above description is that the kinetic traces and transient XAS energy profiles point to a concerted behavior of Br and Pb in response to the optical excitation. The time scales of the intensity decays are fully in line with the Auger[52,53] and PL recombination lifetimes[44,54] in $CsPbBr_3$ perovskites. The relaxation occurs with a direct recovery of the perovskite's ground state, as confirmed by the retention of the TR-XAS line shapes in the decay process and by the time evolution of the *C* parameter.

The high PL quantum yields reported for $CsPbBr_3$ NCs[44] and the fact that the transients do not change line shape profile, i.e., there is no evidence for intermediate states, point to a recovery of the system largely dominated by charge carrier recombination. The presence of polaronic distortions is consistent with this scenario: after the photocarriers have induced the lattice displacements dictated by the strong electron−phonon coupling of the system, the subsequent electron−hole recombination causes the reversible unlocking of the structural distortions of the Pb−Br framework, back to the ground-state configuration.

Notably, spectral line changes as a function of time delay were detected in $Cs_3Bi_2Br_9$ perovskites with Br K-edge TR-XAS as a consequence of their asynchronous electronic and structural relaxation upon optical excitation,[59] with long-persisting lattice disorder after charge carrier recombination. The observation of short-lived valence holes in $Cs_3Bi_2Br_9$, compared to the postedge signatures of lattice distortion, indicates that composition and structure of the inorganic sublattice in halide perovskites, either Bi_2Br_9 or $PbBr_3$, can strongly influence the photodynamics of the system and thus its optoelectronic performances.

This work also highlights the importance of local structural techniques in unraveling the nature of electronic and structural changes in perovskites, triggered by different external perturbations. In diffraction, structural modifications are obtained using approaches that go beyond standard Rietveld refinement methods. One of these methods relies, for example, on the computation of the Fourier transform of the total scattering structure factor to retrieve the PDF, which expresses a probability of finding pairs of atoms separated by a distance *r*.[66] PDF analysis from X-ray powder diffraction in a host of organic perovskites showed significant internal local distortions of the lead halide octahedra at room temperature.[19] Later, total scattering structural characterization, relying on a joint Debye scattering equation/atomic PDF approach, clarified that in $CsPbBr_3$ NCs the structural defectiveness is due to twin boundaries, whose density increase with temperature leads to an apparent higher-symmetry structure that does, however, not correspond to the $Pm\bar{3}m$ cubic phase.[12] A recent high energy resolution inelastic X-ray scattering and PDF study on $MAPbI_3$ pointed to the presence of thermally active anharmonic soft modes at 350 K, corresponding to in-phase and out-of-phase rotations of the PbI_6 octahedra.[11] Shortly after, local polar fluctuations were also confirmed in $MAPbBr_3$ and $CsPbBr_3$ perovskites in a temperature-dependent Raman study, where the presence of a zero-frequency Raman peak was assigned to anharmonic thermal fluctuations among different noncubic structures.[15]

All these studies underline that correlating medium- to long-range structural methods with local probes helps distinguish subtle changes in the perovskite lattice. In this respect, XAS represents a correlative short-range structural tool to probe disordered or dynamically changing systems such as lead halide perovskite NCs. In its time-resolved implementation, TR-XAS offers the advantage of combining electronic and local structural sensitivity, making it an ideal technique to probe lattice modifications induced by the presence of photocarriers, as in the case of polaron formation[32,33,36,59] or charge trapping,[60,67] and to discern them from thermally induced changes.

CONCLUSIONS

We presented results of light- and temperature-induced changes at the Br K-edge and Pb L_3-edge of $CsPbBr_3$ NCs dispersed in toluene solution or as dry powders. Our findings show strong differences between the thermal and optical response of the system, excluding dominant photothermal effects in the observed pump−probe dynamics. The photoinduced spectral changes at the Br K-edge, stemming from a polaron distortion, are here quantified for the first time using advanced band structure calculation, including an *a-priori* selection of the excited state and fully accounting for core-hole effects on the TR-XAS spectra. The comparison between our experiment and theory identifies the lattice changes at the origin of the transient Br postedge modulations with a distortion along an LO phonon mode at 18 meV. These simulations provide an atomic-level description of the light-induced nuclear displacement, dominated by an asymmetric Pb−Br bond shortening along the orthorhombic *c*-axis. This is supported by the identical kinetic evolution of the transient Br K-edge and Pb L_3-edge transients, which show that the latter is a direct consequence of the polaronic distortion around Br centers. This is also consistent

https://doi.org/10.1021/jacs.1c02403
J. Am. Chem. Soc. 2021, 143, 9048−9059

with the high PL quantum yields reported for $CsPbBr_3$ NCs[44] and unravels new microscopic insights in the Pb−Br sublattice dynamics, clarifying the perovskite response under light-induced out-of-equilibrium conditions.

■ ASSOCIATED CONTENT

Supporting Information

The Supporting Information is available free of charge at https://pubs.acs.org/doi/10.1021/jacs.1c02403.

Samples and characterization, experimental methods, fluence scans data analysis, energy scans data analysis, time scans data analysis, estimation of the number of photocarriers, photoinduced blue shift of the Br K-edge, computational methods and DOS calculation, *T*-dependent XRD and XAS (PDF)

■ AUTHOR INFORMATION

Corresponding Authors

Majed Chergui − *Laboratory of Ultrafast Spectroscopy (LSU) and Lausanne Centre for Ultrafast Science (LACUS), École Polytechnique Fédérale de Lausanne, CH-1015 Lausanne, Switzerland;* orcid.org/0000-0002-4856-226X; Email: majed.chergui@epfl.ch

Giulia F. Mancini − *Laboratory of Ultrafast Spectroscopy (LSU) and Lausanne Centre for Ultrafast Science (LACUS), École Polytechnique Fédérale de Lausanne, CH-1015 Lausanne, Switzerland;* Present Address: Department of Physics, University of Pavia, I-27100 Pavia, Italy.; orcid.org/0000-0002-7752-2822; Email: giuliafulvia.mancini@unipv.it

Authors

Oliviero Cannelli − *Laboratory of Ultrafast Spectroscopy (LSU) and Lausanne Centre for Ultrafast Science (LACUS), École Polytechnique Fédérale de Lausanne, CH-1015 Lausanne, Switzerland;* orcid.org/0000-0002-1844-4799

Nicola Colonna − *Laboratory for Neutron Scattering and Imaging, Paul Scherrer Institute, CH-5232 Villigen-PSI, Switzerland; National Centre for Computational Design and Discovery of Novel Materials (MARVEL), École Polytechnique Fédérale de Lausanne, CH-1015 Lausanne, Switzerland;* orcid.org/0000-0002-6106-6316

Michele Puppin − *Laboratory of Ultrafast Spectroscopy (LSU) and Lausanne Centre for Ultrafast Science (LACUS), École Polytechnique Fédérale de Lausanne, CH-1015 Lausanne, Switzerland;* orcid.org/0000-0002-1328-7165

Thomas C. Rossi − *Laboratory of Ultrafast Spectroscopy (LSU) and Lausanne Centre for Ultrafast Science (LACUS), École Polytechnique Fédérale de Lausanne, CH-1015 Lausanne, Switzerland;* Present Address: Department of Chemistry and Materials Research Laboratory, University of Illinois at Urbana−Champaign, Champaign, Illinois 61820, United States.; orcid.org/0000-0002-7448-8948

Dominik Kinschel − *Laboratory of Ultrafast Spectroscopy (LSU) and Lausanne Centre for Ultrafast Science (LACUS), École Polytechnique Fédérale de Lausanne, CH-1015 Lausanne, Switzerland;* orcid.org/0000-0002-0269-8567

Ludmila M. D. Leroy − *Laboratory of Ultrafast Spectroscopy (LSU) and Lausanne Centre for Ultrafast Science (LACUS), École Polytechnique Fédérale de Lausanne, CH-1015 Lausanne, Switzerland; LabCri, Universidade Federal de Minas Gerais, 31270-901 Belo Horizonte, Brazil;* orcid.org/0000-0002-4272-0298

Janina Löffler − *Laboratory of Ultrafast Spectroscopy (LSU) and Lausanne Centre for Ultrafast Science (LACUS), École Polytechnique Fédérale de Lausanne, CH-1015 Lausanne, Switzerland;* orcid.org/0000-0003-3147-8640

James M. Budarz − *Laboratory of Ultrafast Spectroscopy (LSU) and Lausanne Centre for Ultrafast Science (LACUS), École Polytechnique Fédérale de Lausanne, CH-1015 Lausanne, Switzerland;* orcid.org/0000-0002-7673-6626

Anne Marie March − *Chemical Sciences and Engineering Division, Argonne National Laboratory, Lemont, Illinois 60439, United States;* orcid.org/0000-0003-2961-1246

Gilles Doumy − *Chemical Sciences and Engineering Division, Argonne National Laboratory, Lemont, Illinois 60439, United States;* orcid.org/0000-0001-8672-4138

Andre Al Haddad − *Chemical Sciences and Engineering Division, Argonne National Laboratory, Lemont, Illinois 60439, United States;* Present Address: Paul Scherrer Institute (PSI), 5232 Villigen, Switzerland.

Ming-Feng Tu − *Chemical Sciences and Engineering Division, Argonne National Laboratory, Lemont, Illinois 60439, United States;* orcid.org/0000-0001-7834-0329

Yoshiaki Kumagai − *Chemical Sciences and Engineering Division, Argonne National Laboratory, Lemont, Illinois 60439, United States;* orcid.org/0000-0002-2492-4676

Donald Walko − *Advanced Photon Source, Argonne National Laboratory, Lemont, Illinois 60439, United States*

Grigory Smolentsev − *Paul Scherrer Institute (PSI), 5232 Villigen, Switzerland;* orcid.org/0000-0001-7348-7276

Franziska Krieg − *Institute of Inorganic Chemistry, Department of Chemistry and Applied Biosciences, ETH Zürich, CH-8093 Zürich, Switzerland; Laboratory for Thin Films and Photovoltaics, Empa-Swiss Federal Laboratories for Materials Science and Technology, CH-8600 Dübendorf, Switzerland;* orcid.org/0000-0002-0370-1318

Simon C. Boehme − *Institute of Inorganic Chemistry, Department of Chemistry and Applied Biosciences, ETH Zürich, CH-8093 Zürich, Switzerland; Laboratory for Thin Films and Photovoltaics, Empa-Swiss Federal Laboratories for Materials Science and Technology, CH-8600 Dübendorf, Switzerland;* orcid.org/0000-0002-8399-5773

Maksym V. Kovalenko − *Institute of Inorganic Chemistry, Department of Chemistry and Applied Biosciences, ETH Zürich, CH-8093 Zürich, Switzerland; Laboratory for Thin Films and Photovoltaics, Empa-Swiss Federal Laboratories for Materials Science and Technology, CH-8600 Dübendorf, Switzerland;* orcid.org/0000-0002-6396-8938

Complete contact information is available at: https://pubs.acs.org/10.1021/jacs.1c02403

Notes

The authors declare no competing financial interest.

Processed data shown in this manuscript are available in the Supporting Information. Raw Br K-edge and Pb L_3-edge XAS data were generated at APS and SLS large-scale facilities and are available in the repository 10.5281/zenodo.4564629.

■ ACKNOWLEDGMENTS

This work was supported by the European Research Council Advanced Grant H2020 ERCEA 695197 DYNAMOX and by the SwissNSF NCCR-MUST and NCCR-MARVEL. G.F.M.

acknowledges the support of the European Union's Horizon 2020 research and innovation program, through the grant agreement no. 851154 (ULTRAIMAGE). The Argonne group (G.D., A.M.M., A.A., Y.K., M.-F.T.) was supported by the U.S. Department of Energy, Office of Science, Basic Energy Sciences, Chemical Sciences, Geosciences, and Biosciences Division, under contract DE-AC02-06CH11357. This research used resources of the Advanced Photon Source, a U.S. Department of Energy (DOE) Office of Science User Facility operated for the DOE Office of Science by Argonne National Laboratory under Contract No. DE-AC02-06CH11357. M.K. acknowledges funding by the European Union's Horizon 2020 program, through a FET Open research and innovation action under the grant agreement no. 899141 (PoLLoC). S.C.B. acknowledges The Netherlands Organization of Scientific Research (NWO) for financial support through the Innovational Research Incentives (Veni) Scheme (722.017.011).

REFERENCES

(1) Liu, X.-K.; Xu, W.; Bai, S.; Jin, Y.; Wang, J.; Friend, R. H.; Gao, F. Metal Halide Perovskites for Light-Emitting Diodes. *Nat. Mater.* **2021**, *20*, 1−12.

(2) Sutherland, B. R.; Sargent, E. H. Perovskite Photonic Sources. *Nat. Photonics* **2016**, *10* (5), 295−302.

(3) Fang, Y.; Dong, Q.; Shao, Y.; Yuan, Y.; Huang, J. Highly Narrowband Perovskite Single-Crystal Photodetectors Enabled by Surface-Charge Recombination. *Nat. Photonics* **2015**, *9* (10), 679−686.

(4) Su, R.; Ghosh, S.; Wang, J.; Liu, S.; Diederichs, C.; Liew, T. C. H.; Xiong, Q. Observation of Exciton Polariton Condensation in a Perovskite Lattice at Room Temperature. *Nat. Phys.* **2020**, *16* (3), 301−306.

(5) Utzat, H.; Sun, W.; Kaplan, A. E. K.; Krieg, F.; Ginterseder, M.; Spokoyny, B.; Klein, N. D.; Shulenberger, K. E.; Perkinson, C. F.; Kovalenko, M. V.; Bawendi, M. G. Coherent Single-Photon Emission from Colloidal Lead Halide Perovskite Quantum Dots. *Science* **2019**, *363* (6431), 1068−1072.

(6) Akkerman, Q. A.; Rainò, G.; Kovalenko, M. V.; Manna, L. Genesis, Challenges and Opportunities for Colloidal Lead Halide Perovskite Nanocrystals. *Nat. Mater.* **2018**, *17* (5), 394−405.

(7) Xing, G.; Mathews, N.; Sun, S.; Lim, S. S.; Lam, Y. M.; Grätzel, M.; Mhaisalkar, S.; Sum, T. C. Long-Range Balanced Electron- and Hole-Transport Lengths in Organic-Inorganic $CH_3NH_3PbI_3$. *Science* **2013**, *342* (6156), 344−347.

(8) Stranks, S. D.; Eperon, G. E.; Grancini, G.; Menelaou, C.; Alcocer, M. J. P.; Leijtens, T.; Herz, L. M.; Petrozza, A.; Snaith, H. J. Electron-Hole Diffusion Lengths Exceeding 1 Micrometer in an Organometal Trihalide Perovskite Absorber. *Science* **2013**, *342* (6156), 341−344.

(9) Herz, L. M. Charge-Carrier Dynamics in Organic-Inorganic Metal Halide Perovskites. *Annu. Rev. Phys. Chem.* **2016**, *67* (1), 65−89.

(10) Miyata, K.; Atallah, T. L.; Zhu, X.-Y. Lead Halide Perovskites: Crystal-Liquid Duality, Phonon Glass Electron Crystals, and Large Polaron Formation. *Sci. Adv.* **2017**, *3* (10), No. e1701469.

(11) Beecher, A. N.; Semonin, O. E.; Skelton, J. M.; Frost, J. M.; Terban, M. W.; Zhai, H.; Alatas, A.; Owen, J. S.; Walsh, A.; Billinge, S. J. L. Direct Observation of Dynamic Symmetry Breaking above Room Temperature in Methylammonium Lead Iodide Perovskite. *ACS Energy Lett.* **2016**, *1* (4), 880−887.

(12) Bertolotti, F.; Protesescu, L.; Kovalenko, M. V.; Yakunin, S.; Cervellino, A.; Billinge, S. J. L.; Terban, M. W.; Pedersen, J. S.; Masciocchi, N.; Guagliardi, A. Coherent Nanotwins and Dynamic Disorder in Cesium Lead Halide Perovskite Nanocrystals. *ACS Nano* **2017**, *11* (4), 3819−3831.

(13) Cottingham, P.; Brutchey, R. L. Depressed Phase Transitions and Thermally Persistent Local Distortions in $CsPbBr_3$ Quantum Dots. *Chem. Mater.* **2018**, *30* (19), 6711−6716.

(14) Miyata, K.; Meggiolaro, D.; Trinh, M. T.; Joshi, P. P.; Mosconi, E.; Jones, S. C.; Angelis, F. D.; Zhu, X.-Y. Large Polarons in Lead Halide Perovskites. *Sci. Adv.* **2017**, *3* (8), No. e1701217.

(15) Yaffe, O.; Guo, Y.; Tan, L. Z.; Egger, D. A.; Hull, T.; Stoumpos, C. C.; Zheng, F.; Heinz, T. F.; Kronik, L.; Kanatzidis, M. G.; Owen, J. S.; Rappe, A. M.; Pimenta, M. A.; Brus, L. E. Local Polar Fluctuations in Lead Halide Perovskite Crystals. *Phys. Rev. Lett.* **2017**, *118* (13), 136001.

(16) Stoumpos, C. C.; Malliakas, C. D.; Peters, J. A.; Liu, Z.; Sebastian, M.; Im, J.; Chasapis, T. C.; Wibowo, A. C.; Chung, D. Y.; Freeman, A. J.; Wessels, B. W.; Kanatzidis, M. G. Crystal Growth of the Perovskite Semiconductor $CsPbBr_3$: A New Material for High-Energy Radiation Detection. *Cryst. Growth Des.* **2013**, *13* (7), 2722−2727.

(17) Kovalenko, M. V.; Protesescu, L.; Bodnarchuk, M. I. Properties and Potential Optoelectronic Applications of Lead Halide Perovskite Nanocrystals. *Science* **2017**, *358* (6364), 745−750.

(18) Fujii, Y.; Hoshino, S.; Yamada, Y.; Shirane, G. Neutron-Scattering Study on Phase Transitions of $CsPbCl_3$. *Phys. Rev. B* **1974**, *9* (10), 4549−4559.

(19) Worhatch, R. J.; Kim, H.; Swainson, I. P.; Yonkeu, A. L.; Billinge, S. J. L. Study of Local Structure in Selected Organic-Inorganic Perovskites in the $Pm\bar{3}m$ Phase. *Chem. Mater.* **2008**, *20* (4), 1272−1277.

(20) Bernasconi, A.; Malavasi, L. Direct Evidence of Permanent Octahedra Distortion in $MAPbBr_3$ Hybrid Perovskite. *ACS Energy Lett.* **2017**, *2* (4), 863−868.

(21) Richter, J. M.; Branchi, F.; Valduga de Almeida Camargo, F.; Zhao, B.; Friend, R. H.; Cerullo, G.; Deschler, F. Ultrafast Carrier Thermalization in Lead Iodide Perovskite Probed with Two-Dimensional Electronic Spectroscopy. *Nat. Commun.* **2017**, *8* (1), 376.

(22) Hopper, T. R.; Gorodetsky, A.; Jeong, A.; Krieg, F.; Bodnarchuk, M. I.; Maimaris, M.; Chaplain, M.; Macdonald, T. J.; Huang, X.; Lovrincic, R.; Kovalenko, M. V.; Bakulin, A. A. Hot Carrier Dynamics in Perovskite Nanocrystal Solids: Role of the Cold Carriers, Nanoconfinement, and the Surface. *Nano Lett.* **2020**, *20* (4), 2271−2278.

(23) Boehme, S. C.; Brinck, S. t.; Maes, J.; Yazdani, N.; Zapata, F.; Chen, K.; Wood, V.; Hodgkiss, J. M.; Hens, Z.; Geiregat, P.; Infante, I. Phonon-Mediated and Weakly Size-Dependent Electron and Hole Cooling in $CsPbBr_3$ Nanocrystals Revealed by Atomistic Simulations and Ultrafast Spectroscopy. *Nano Lett.* **2020**, *20*, 1819.

(24) Seiler, H.; Palato, S.; Sonnichsen, C.; Baker, H.; Socie, E.; Strandell, D. P.; Kambhampati, P. Two-Dimensional Electronic Spectroscopy Reveals Liquid-like Lineshape Dynamics in $CsPbI_3$ Perovskite Nanocrystals. *Nat. Commun.* **2019**, *10* (1), 4962.

(25) Batignani, G.; Fumero, G.; Kandada, A. R. S.; Cerullo, G.; Gandini, M.; Ferrante, C.; Petrozza, A.; Scopigno, T. Probing Femtosecond Lattice Displacement upon Photo-Carrier Generation in Lead Halide Perovskite. *Nat. Commun.* **2018**, *9* (1), 1−5.

(26) Zhao, W.; Qin, Z.; Zhang, C.; Wang, G.; Dai, X.; Xiao, M. Coherent Exciton-Phonon Coupling in Perovskite Semiconductor Nanocrystals Studied by Two-Dimensional Electronic Spectroscopy. *Appl. Phys. Lett.* **2019**, *115* (24), 243101.

(27) Cinquanta, E.; Meggiolaro, D.; Motti, S. G.; Gandini, M.; Alcocer, M. J. P.; Akkerman, Q. A.; Vozzi, C.; Manna, L.; De Angelis, F.; Petrozza, A.; Stagira, S. Ultrafast THz Probe of Photoinduced Polarons in Lead-Halide Perovskites. *Phys. Rev. Lett.* **2019**, *122* (16), 166601.

(28) Zhu, X.-Y.; Podzorov, V. Charge Carriers in Hybrid Organic-Inorganic Lead Halide Perovskites Might Be Protected as Large Polarons. *J. Phys. Chem. Lett.* **2015**, *6* (23), 4758−4761.

(29) Yu, P.; Cardona, M. *Fundamentals of Semiconductors: Physics and Materials Properties*; Springer Science & Business Media, 2010.

(30) Wright, A. D.; Verdi, C.; Milot, R. L.; Eperon, G. E.; Pérez-Osorio, M. A.; Snaith, H. J.; Giustino, F.; Johnston, M. B.; Herz, L. M. Electron-Phonon Coupling in Hybrid Lead Halide Perovskites. *Nat. Commun.* **2016**, *7* (1), 11755.

(31) Ramade, J.; Andriambariarijaona, L. M.; Steinmetz, V.; Goubet, N.; Legrand, L.; Barisien, T.; Bernardot, F.; Testelin, C.; Lhuillier, E.; Bramati, A.; Chamarro, M. Exciton-Phonon Coupling in a $CsPbBr_3$ Single Nanocrystal. *Appl. Phys. Lett.* **2018**, *112* (7), 072104.

https://doi.org/10.1021/jacs.1c02403
J. Am. Chem. Soc. 2021, 143, 9048−9059

(32) Zheng, K.; Abdellah, M.; Zhu, Q.; Kong, Q.; Jennings, G.; Kurtz, C. A.; Messing, M. E.; Niu, Y.; Gosztola, D. J.; Al-Marri, M. J.; Zhang, X.; Pullerits, T.; Canton, S. E. Direct Experimental Evidence for Photoinduced Strong-Coupling Polarons in Organolead Halide Perovskite Nanoparticles. *J. Phys. Chem. Lett.* **2016**, *7* (22), 4535−4539.
(33) Liu, C.; Tsai, H.; Nie, W.; Gosztola, D. J.; Zhang, X. Direct Spectroscopic Observation of the Hole Polaron in Lead Halide Perovskites. *J. Phys. Chem. Lett.* **2020**, *11* (15), 6256−6261.
(34) Wu, X.; Tan, L. Z.; Shen, X.; Hu, T.; Miyata, K.; Trinh, M. T.; Li, R.; Coffee, R.; Liu, S.; Egger, D. A.; Makasyuk, I.; Zheng, Q.; Fry, A.; Robinson, J. S.; Smith, M. D.; Guzelturk, B.; Karunadasa, H. I.; Wang, X.; Zhu, X.; Kronik, L.; Rappe, A. M.; Lindenberg, A. M. Light-Induced Picosecond Rotational Disordering of the Inorganic Sublattice in Hybrid Perovskites. *Sci. Adv.* **2017**, *3* (7), No. e1602388.
(35) Guzelturk, B.; Winkler, T.; Van de Goor, T. W. J.; Smith, M. D.; Bourelle, S. A.; Feldmann, S.; Trigo, M.; Teitelbaum, S. W.; Steinrück, H.-G.; de la Pena, G. A.; Alonso-Mori, R.; Zhu, D.; Sato, T.; Karunadasa, H. I.; Toney, M. F.; Deschler, F.; Lindenberg, A. M. Visualization of Dynamic Polaronic Strain Fields in Hybrid Lead Halide Perovskites. *Nat. Mater.* **2021**, *20*, 1−6.
(36) Santomauro, F. G.; Grilj, J.; Mewes, L.; Nedelcu, G.; Yakunin, S.; Rossi, T.; Capano, G.; Al Haddad, A.; Budarz, J.; Kinschel, D.; Ferreira, D. S.; Rossi, G.; Gutierrez Tovar, M.; Grolimund, D.; Samson, V.; Nachtegaal, M.; Smolentsev, G.; Kovalenko, M. V.; Chergui, M. Localized Holes and Delocalized Electrons in Photoexcited Inorganic Perovskites: Watching Each Atomic Actor by Picosecond X-Ray Absorption Spectroscopy. *Struct. Dyn.* **2017**, *4* (4), 044002.
(37) Kirschner, M. S.; Diroll, B. T.; Guo, P.; Harvey, S. M.; Helweh, W.; Flanders, N. C.; Brumberg, A.; Watkins, N. E.; Leonard, A. A.; Evans, A. M.; Wasielewski, M. R.; Dichtel, W. R.; Zhang, X.; Chen, L. X.; Schaller, R. D. Photoinduced, Reversible Phase Transitions in All-Inorganic Perovskite Nanocrystals. *Nat. Commun.* **2019**, *10* (1), 504.
(38) Puppin, M.; Polishchuk, S.; Colonna, N.; Crepaldi, A.; Dirin, D. N.; Nazarenko, O.; De Gennaro, R.; Gatti, G.; Roth, S.; Barillot, T.; Poletto, L.; Xian, R. P.; Rettig, L.; Wolf, M.; Ernstorfer, R.; Kovalenko, M. V.; Marzari, N.; Grioni, M.; Chergui, M. Evidence of Large Polarons in Photoemission Band Mapping of the Perovskite Semiconductor $CsPbBr_3$. *Phys. Rev. Lett.* **2020**, *124* (20), 206402.
(39) Rehr, J. J.; Albers, R. C. Theoretical Approaches to X-Ray Absorption Fine Structure. *Rev. Mod. Phys.* **2000**, *72* (3), 621−654.
(40) Teo, B. K. *EXAFS: Basic Principles and Data Analysis*; Springer Science & Business Media, 2012.
(41) Chergui, M.; Collet, E. Photoinduced Structural Dynamics of Molecular Systems Mapped by Time-Resolved X-Ray Methods. *Chem. Rev.* **2017**, *117* (16), 11025−11065.
(42) March, A. M.; Stickrath, A.; Doumy, G.; Kanter, E. P.; Krässig, B.; Southworth, S. H.; Attenkofer, K.; Kurtz, C. A.; Chen, L. X.; Young, L. Development of High-Repetition-Rate Laser Pump/x-Ray Probe Methodologies for Synchrotron Facilities. *Rev. Sci. Instrum.* **2011**, *82* (7), 073110.
(43) March, A. M.; Doumy, G.; Andersen, A.; Al Haddad, A.; Kumagai, Y.; Tu, M.-F.; Bang, J.; Bostedt, C.; Uhlig, J.; Nascimento, D. R.; Assefa, T. A.; Németh, Z.; Vankó, G.; Gawelda, W.; Govind, N.; Young, L. Elucidation of the Photoaquation Reaction Mechanism in Ferrous Hexacyanide Using Synchrotron X-Rays with Sub-Pulse-Duration Sensitivity. *J. Chem. Phys.* **2019**, *151* (14), 144306.
(44) Krieg, F.; Ochsenbein, S. T.; Yakunin, S.; Ten Brinck, S.; Aellen, P.; Süess, A.; Clerc, B.; Guggisberg, D.; Nazarenko, O.; Shynkarenko, Y.; Kumar, S.; Shih, C.-J.; Infante, I.; Kovalenko, M. V. Colloidal $CsPbX_3$ (X = Cl, Br, I) Nanocrystals 2.0: Zwitterionic Capping Ligands for Improved Durability and Stability. *ACS Energy Lett.* **2018**, *3* (3), 641−646.
(45) Giannozzi, P.; Baroni, S.; Bonini, N.; Calandra, M.; Car, R.; Cavazzoni, C.; Ceresoli, D.; Chiarotti, G. L.; Cococcioni, M.; Dabo, I.; Corso, A. D.; Gironcoli, S.; de Fabris, S.; Fratesi, G.; Gebauer, R.; Gerstmann, U.; Gougoussis, C.; Kokalj, A.; Lazzeri, M.; Martin-Samos, L.; Marzari, N.; Mauri, F.; Mazzarello, R.; Paolini, S.; Pasquarello, A.; Paulatto, L.; Sbraccia, C.; Scandolo, S.; Sclauzero, G.; Seitsonen, A. P.; Smogunov, A.; Umari, P.; Wentzcovitch, R. M. QUANTUM ESPRESSO: A Modular and Open-Source Software Project for Quantum Simulations of Materials. *J. Phys.: Condens. Matter* **2009**, *21* (39), 395502.
(46) Giannozzi, P.; Andreussi, O.; Brumme, T.; Bunau, O.; Nardelli, M. B.; Calandra, M.; Car, R.; Cavazzoni, C.; Ceresoli, D.; Cococcioni, M.; Colonna, N.; Carnimeo, I.; Corso, A. D.; Gironcoli, S.; de Delugas, P.; DiStasio, R. A.; Ferretti, A.; Floris, A.; Fratesi, G.; Fugallo, G.; Gebauer, R.; Gerstmann, U.; Giustino, F.; Gorni, T.; Jia, J.; Kawamura, M.; Ko, H.-Y.; Kokalj, A.; Küçükbenli, E.; Lazzeri, M.; Marsili, M.; Marzari, N.; Mauri, F.; Nguyen, N. L.; Nguyen, H.-V.; Otero-De-La-Roza, A.; Paulatto, L.; Poncé, S.; Rocca, D.; Sabatini, R.; Santra, B.; Schlipf, M.; Seitsonen, A. P.; Smogunov, A.; Timrov, I.; Thonhauser, T.; Umari, P.; Vast, N.; Wu, X.; Baroni, S. Advanced Capabilities for Materials Modelling with Quantum ESPRESSO. *J. Phys.: Condens. Matter* **2017**, *29* (46), 465901.
(47) Perdew, J. P.; Burke, K.; Ernzerhof, M. Generalized Gradient Approximation Made Simple. *Phys. Rev. Lett.* **1996**, *77* (18), 3865−3868.
(48) Dal Corso, A. Pseudopotentials Periodic Table: From H to Pu. *Comput. Mater. Sci.* **2014**, *95*, 337−350.
(49) Taillefumier, M.; Cabaret, D.; Flank, A.-M.; Mauri, F. X-Ray Absorption near-Edge Structure Calculations with the Pseudopotentials: Application to the *K* Edge in Diamond and α-Quartz. *Phys. Rev. B: Condens. Matter Mater. Phys.* **2002**, *66* (19), 195107.
(50) Gougoussis, C.; Calandra, M.; Seitsonen, A. P.; Mauri, F. First-principles calculations of X-ray absorption in a scheme based on ultrasoft pseudopotentials: From α-quartz to high-T_c compounds. *Phys. Rev. B: Condens. Matter Mater. Phys.* **2009**, *80* (7), 075102.
(51) Gilmore, K.; Vinson, J.; Shirley, E. L.; Prendergast, D.; Pemmaraju, C. D.; Kas, J. J.; Vila, F. D.; Rehr, J. J. Efficient Implementation of Core-Excitation Bethe-Salpeter Equation Calculations. *Comput. Phys. Commun.* **2015**, *197*, 109−117.
(52) Wang, Y.; Li, X.; Song, J.; Xiao, L.; Zeng, H.; Sun, H. All-Inorganic Colloidal Perovskite Quantum Dots: A New Class of Lasing Materials with Favorable Characteristics. *Adv. Mater.* **2015**, *27* (44), 7101−7108.
(53) Diroll, B. T.; Schaller, R. D. Intraband Cooling in All-Inorganic and Hybrid Organic-Inorganic Perovskite Nanocrystals. *Adv. Funct. Mater.* **2019**, *29* (37), 1901725.
(54) Ahmed, T.; Seth, S.; Samanta, A. Boosting the Photoluminescence of $CsPbX_3$ (X = Cl, Br, I) Perovskite Nanocrystals Covering a Wide Wavelength Range by Postsynthetic Treatment with Tetrafluoroborate Salts. *Chem. Mater.* **2018**, *30* (11), 3633−3637.
(55) Hopper, T. R.; Gorodetsky, A.; Frost, J. M.; Müller, C.; Lovrincic, R.; Bakulin, A. A. Ultrafast Intraband Spectroscopy of Hot-Carrier Cooling in Lead-Halide Perovskites. *ACS Energy Lett.* **2018**, *3* (9), 2199−2205.
(56) Diroll, B. T.; Schaller, R. D. Heating and Cooling of Ligand-Coated Colloidal Nanocrystals in Solid Films and Solvent Matrices. *Nanoscale* **2019**, *11* (17), 8204−8209.
(57) Prendergast, D.; Galli, G. X-Ray Absorption Spectra of Water from First Principles Calculations. *Phys. Rev. Lett.* **2006**, *96* (21), 215502.
(58) Gao, S.-P.; Pickard, C. J.; Payne, M. C.; Zhu, J.; Yuan, J. Theory of Core-Hole Effects in 1s Core-Level Spectroscopy of the First-Row Elements. *Phys. Rev. B: Condens. Matter Mater. Phys.* **2008**, *77* (11), 115122.
(59) Liu, C.; Wang, Y.; Geng, H.; Zhu, T.; Ertekin, E.; Gosztola, D.; Yang, S.; Huang, J.; Yang, B.; Han, K.; Canton, S. E.; Kong, Q.; Zheng, K.; Zhang, X. Asynchronous Photoexcited Electronic and Structural Relaxation in Lead-Free Perovskites. *J. Am. Chem. Soc.* **2019**, *141* (33), 13074−13080.
(60) Penfold, T. J.; Szlachetko, J.; Santomauro, F. G.; Britz, A.; Gawelda, W.; Doumy, G.; March, A. M.; Southworth, S. H.; Rittmann, J.; Abela, R.; Chergui, M.; Milne, C. J. Revealing Hole Trapping in Zinc Oxide Nanoparticles by Time-Resolved X-Ray Spectroscopy. *Nat. Commun.* **2018**, *9* (1), 478.
(61) Koide, A.; Uemura, Y.; Kido, D.; Wakisaka, Y.; Takakusagi, S.; Ohtani, B.; Niwa, Y.; Nozawa, S.; Ichiyanagi, K.; Fukaya, R.; Adachi, S.;

https://doi.org/10.1021/jacs.1c02403
J. Am. Chem. Soc. 2021, 143, 9048−9059

Katayama, T.; Togashi, T.; Owada, S.; Yabashi, M.; Yamamoto, Y.; Katayama, M.; Hatada, K.; Yokoyama, T.; Asakura, K. Photoinduced Anisotropic Distortion as the Electron Trapping Site of Tungsten Trioxide by Ultrafast W L_1-Edge X-Ray Absorption Spectroscopy with Full Potential Multiple Scattering Calculations. *Phys. Chem. Chem. Phys.* **2020**, *22* (5), 2615−2621.

(62) Ong, W.-L.; Rupich, S. M.; Talapin, D. V.; McGaughey, A. J. H.; Malen, J. A. Surface Chemistry Mediates Thermal Transport in Three-Dimensional Nanocrystal Arrays. *Nat. Mater.* **2013**, *12* (5), 410−415.

(63) Diroll, B. T.; Mannodi-Kanakkithodi, A.; Chan, M. K. Y.; Schaller, R. D. Spectroscopic Comparison of Thermal Transport at Organic-Inorganic and Organic-Hybrid Interfaces Using $CsPbBr_3$ and $FAPbBr_3$ (FA = Formamidinium) Perovskite Nanocrystals. *Nano Lett.* **2019**, *19* (11), 8155−8160.

(64) Limmer, D. T.; Ginsberg, N. S. Photoinduced Phase Separation in the Lead Halides Is a Polaronic Effect. *J. Chem. Phys.* **2020**, *152* (23), 230901.

(65) Ramade, J.; Andriambariarijaona, L. M.; Steinmetz, V.; Goubet, N.; Legrand, L.; Barisien, T.; Bernardot, F.; Testelin, C.; Lhuillier, E.; Bramati, A.; Chamarro, M. Exciton-Phonon Coupling in a $CsPbBr_3$ Single Nanocrystal. *Appl. Phys. Lett.* **2018**, *112* (7), 072104.

(66) Egami, T.; Billinge, S. J. L. *Underneath the Bragg Peaks: Structural Analysis of Complex Materials*; Newnes, 2012.

(67) Rittmann-Frank, M. H.; Milne, C. J.; Rittmann, J.; Reinhard, M.; Penfold, T. J.; Chergui, M. Mapping of the Photoinduced Electron Traps in TiO_2 by Picosecond X-Ray Absorption Spectroscopy. *Angew. Chem., Int. Ed.* **2014**, *53* (23), 5858−5862.

(68) Momma, K.; Izumi, F. VESTA 3 for Three-Dimensional Visualization of Crystal, Volumetric and Morphology Data. *J. Appl. Crystallogr.* **2011**, *44* (6), 1272−1276.

https://doi.org/10.1021/jacs.1c02403
J. Am. Chem. Soc. 2021, 143, 9048−9059